



Tunable Plasmonic Thermal Emitter Using Metal-Coated Elastomeric Structures

Item Type	thesis
Authors	Zando, Robert
DOI	10.7275/8558646
Download date	2025-02-16 14:34:16
Link to Item	https://hdl.handle.net/20.500.14394/33392

Tunable Plasmonic Thermal Emitter Using Metal-Coated Elastomeric Structures

A Thesis Presented

by

ROBERT ZANDO

Submitted to the Graduate School of the
University of Massachusetts Amherst in partial fulfillment
of the requirements for the degree of

MASTER OF SCIENCE IN MECHANICAL ENGINEERING

May 2016

Department of Mechanical and Industrial Engineering

© Copyright by Robert B. Zando 2016
All Rights Reserved

Tunable Plasmonic Thermal Emitter Using Metal-Coated Elastomeric Structures

A Thesis Presented

by

ROBERT ZANDO

Approved as to style and content by:

Jae-Hawng Lee, Committee Chairperson

Stephen Nonnenmann, Member

Jon McGowan, Member

Sundar Krishnamurty, Department Head
Department of Mechanical and Industrial Engineering

ACKNOWLEDGMENTS

I would like to extend my most sincere gratitude to my adviser Jae-Hwang Lee, whose guidance and patience over the past year made my success in the MIE Master's Program possible. Special thanks as well to my colleagues and friends: Amir Kazemi Moridani, a fellow member of the Lee Research Group, whose assistance in the operation of the FTIR spectrometer and analysis of the resulting spectra were invaluable to my work; and Wanting Xie, whose expertise with the Physics Department SEM allowed me to accurately measure the dimensions of my structure. Thanks are due as well to the University of Massachusetts, which took a chance two years ago by accepting me into the program and thereby offered me the chance to interact with a truly excellent engineering faculty and gain a wide variety of exposure to fields of work I had never even considered in the past.

Finally, special mention to all the support offered to me over the years by my family. To my parents, Mark and Mary Zando, who instilled in me a love of education and a passion for scientific knowledge. My sister, Anne Zando, who has always been there for me when I needed her. And a particularly noteworthy "thank you" to my grandmother, Susan Zando, whose support these past two years (both moral and financial) were essential to my ability to join and succeed in such a rigorous academic program.

ABSTRACT

TUNABLE PLASMONIC THERMAL EMITTER USING METAL-COATED ELASTOMERIC STRUCTURES

MAY 2016

ROBERT ZANDO, B.S., CASE WESTERN RESERVE UNIVERSITY

M.S.M.E., UNIVERSITY OF MASSACHUSETTS AMHERST

Directed by: Professor Jae-Hawng Lee

This project was focused on the creation of a gold-coated grating structure capable of inducing a surface plasmon polariton within the mid-infrared region, enhancing emissions at specific wavelengths based on the grating periodicity. The grating structure was formed on a silicone elastomer, polydimethylsiloxane (PDMS), in order to give the structure, the ability to have the periodicity dimensions of the grating altered by applying a stress, thereby changing the location of the emission enhancement, giving the device the potential to be used as an infrared strain sensor.

Creation of the structure employed a top-down, micro-scale fabrication technique referred to as Direct Laser Writing (DLW). Using a light-sensitive, negative-tone photoresist material, a grating was patterned onto a glass substrate via photopolymerization, in which areas exposed to an ultraviolet (UV) laser were rendered insoluble by forming cross-links on the portions of the resist which interacted with the UV source. This grating was then placed under a custom-designed mold which was then filled with liquid PDMS and cured for 3 hours at 60°C to cure (harden or cross-link) and leaving an inverse elastomer pattern behind once the cured PDMS was peeled off the substrate.

Upon coating the structure with a ~80 nm thick layer of gold, a Fourier Transform infrared (FTIR) spectrometer was used to measure the thermal emissions spectrum of the sample grating at a high temperature (~200°C) and under different strains. These spectra were then analyzed to look for

selective emission enhancements caused by the grating structure due to the inducing of a surface plasmon polariton (SPP), as well as changes in the location and nature of these enhancements based on applied strains. Final results showed two sets of enhancement behaviors with the application of uniaxial strain: a shifting of the region of peak emission enhancement to higher wavelengths, and a broadening of the region of enhancement. However, more testing is needed in order to determine the precise causes of the behavior and to quantify it in such a way that it could be turned into a functioning sensor device.

TABLE OF CONTENTS

	Page
ACKNOWLEDGMENTS.....	iv
ABSTRACTv
LIST OF FIGURES.....	viii
CHAPTER	
1. INTRODUCTION.....	1
1.1 Study Aims	1
1.2 Surface Plasmon Polariton.....	2
1.3 Fresnel's Equations	2
1.4 Momentum Matching	6
1.4.1 Kretschmann and Otto Configurations	7
1.4.2 Grating Method.....	9
1.5 Thermal Radiation and Kirchoff's Law	10
2. METHODS.....	13
2.1 Photolithography	13
2.1.1 Photopolymerization.....	15
2.2 Direct Laser Writing	16
2.3 Sputter Coating	18
2.4 FTIR Spectroscopy	20
3. PREPARATION AND TESTING	24
3.1 Control Scheme	26
3.1.1 Newport Positioners.....	27
3.2 Peel-Off and Sputter Coating	33
3.3 Uniaxial Strain Due to Bending.....	35
4. RESULTS	37
4.1 Crack Testing	39
4.2 Characterization of Thermal Emissions.....	42
5. CONCLUSIONS AND FUTURE WORK.....	46
BIBLIOGRAPHY	49

LIST OF FIGURES

Page

Figure 1: P-Polarized Light.....	3
Figure 2: Dispersion relationship between angular frequency and wave number.	7
Figure 3: The Kretschmann Configuration	8
Figure 4: The Otto Configuration	9
Figure 5: Grating method.....	10
Figure 6: Emissions spectrum of a blackbody	11
Figure 7: Basic photolithography process	15
Figure 8: Soft-lithography process.....	15
Figure 9: DLW concept.....	17
Figure 10: Gaussian Intensity Profile.....	18
Figure 11: Sputter Coat Concept.....	20
Figure 12: Michelson Interferometer	21
Figure 13: Fourier Transform.....	23
Figure 14: The Mai Tai DLW Set-Up	25
Figure 15: Custom LabVIEW Program 1 GUI	28
Figure 16: Custom LabVIEW Program 2 GUI	30
Figure 17: PDMS mold.....	33
Figure 18: Denton Vacuum Sputter Coater	34
Figure 19: Gold coated elastic grating.....	34
Figure 20: Bending.....	35
Figure 20a: Bending Curve	36
Figure 21: Gold-coated grating	38
Figure 22: SEM.....	39
Figure 23: Crack Testing.....	40
Figure 24: Crack Test Results	41
Figure 25: Test Orientations	43
Figure 26: Sample 4 emission contour plot	44
Figure 27: Sample 19 emission contour plot	45

CHAPTER 1 INTRODUCTION

Scientists and engineers have been exploring the potential applications of materials capable of manipulating the electromagnetic spectrum for over a century. In recent years, techniques for directly manipulating materials on a micrometer scale allow for direct, high-precision manipulation of electromagnetic (EM) radiation in ways previously unimagined. From the creation of high-performance reflectors to the production of photonic crystals capable of directly affecting the propagation of radiation through space, the possibilities opened up by the manipulation of materials on a micron scale are truly vast. Among the most intriguing of these artificial phenomena, however, is that of the surface plasmon polariton (SPP), a combination oscillation of electron particles across the surface of a conductor (plasmon) and localized, exponentially decaying electromagnetic field (polariton). Induced by radiation interacting with the barrier of a dielectric and a conductor, the effects are easily detected and numerous in application.

1.1 Study Aims

Sensors utilizing SPP have been utilized for years as a method of analyzing unknown chemicals and material in an area immediately adjacent to the device. (Ruffato et al. 2012) Differences in atmospheric composition alter the properties of the emissions spectrum produced by the SPP and the frequency conditions at which an SPP might be produced (referred to as a Surface Plasmon Resonance frequency). This study, however, aimed to explore the changes that can be induced to the properties of an SPP at mid-IR wavelengths as a result of the deformation caused by uniaxial strains, with the ultimate aim being to produce a practical device capable of acting as an IR strain sensor by quantifying the shift in characteristic emission enhancement via applied strains.

1.2 Surface Plasmon Polariton

Surface plasmons are most broadly described as quanta of the collective oscillation of a group of electrons across the interface between a conductive and dielectric surface. This phenomenon is incited by the interaction of electromagnetic radiation at the interface of two materials with refractive indices of different signs. The entire phenomenon, referred to as an SPP is composed of two components: the collective oscillation of a group of electrons at the location of interaction between the electromagnetic wave and the boundary between the two medium (the “Plasmon”) and the transverse electric field produced by the oscillation which decays exponentially along the surface of the conductive material (the “Polariton”). Because this effect is confined to the surface of the conductive medium, this produces a signal enhancement of the electromagnetic field at the boundary between the conductive surface and the dielectric surface. (Homola et al. 1999)

1.3 Fresnel's Equations

There are a number of relations which provide a mathematical representation of the means by which electromagnetic radiation may excite an oscillation of surface electrons at the interface between a dielectric material and a conductive material. Fresnel's equations provide a comprehensive treatment of this subject (in conjunction with the Maxwell equations). These equations may be derived by considering a light-wave interacting with the interface between two mediums (see Figure 1). When the wave is incident with the boundary, a portion of the radiation will be reflected from the boundary surface, and the remainder will be transmitted through the boundary surface. The angle of the radiation transmitted obeys Snell's law:

$$\sin(\Theta_i)/\sin(\Theta_t) = n_2/n_1$$

where Θ_i is the angle of incidence, Θ_r is the angle of reflected radiation, n_2 is the refractive index of medium 2, and n_1 is the refractive index of medium 1, while the angle of reflection Θ_r is equal to the angle of incidence.

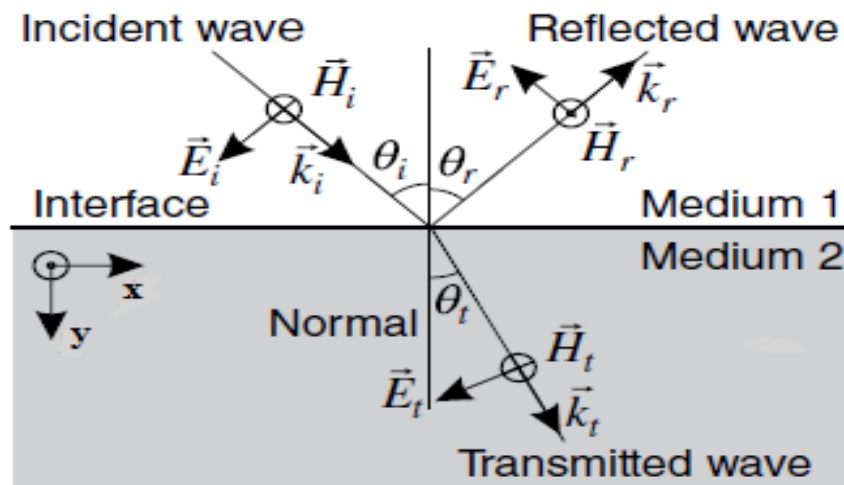


Figure 1: P-Polarized Light

P-Polarized light incident with a boundary between a two media of different refractive indices (Lvovsky 2013)

This relation may also be expressed in terms of the k-vector:

$\vec{k} = (k_x, k_y)$, as $k_{x1} = k_{x2} = k_x$, the magnitude of which is

$$k = \sqrt{k_x^2 + k_y^2} = n(2\pi/\lambda) = n\omega/c$$

where λ is the wavelength in a vacuum, c is the EM-wave velocity in a vacuum, and n is the refractive index of the propagation medium. Each of these waves (transmitted and reflected)

have a wave amplitude of E_i and E_r , the values of which are the ultimate objective of a derived Fresnel Equation. Because electromagnetic radiation is a transverse wave, it is actually composed of two wave components based on the direction of EM oscillation: p-polarized oscillation (oscillating parallel to the plane of incidence) and s-polarized (oscillating perpendicular to the plane of incidence). However, surface plasmons can only be induced by an electric field with an E component parallel to the interface between a dielectric and conductive material (i.e. p-polarized). Therefore, the remainder of this discussion will be concerned only with the p-polarized components of the Fresnel Equations.

The next step is to apply the boundary condition of an electric and magnetic waves at the interface between two mediums, specifically that the components of these fields which are tangent to the surface are continuous across the boundary of the interface. This boundary condition is represented mathematically as:

$$E_i \cos(\Theta_i) + E_r \cos(\Theta_r) = E_t \cos(\Theta_t)$$

for the electric field components and as

$$H_i - H_r = H_t$$

for the magnetic field components.

Since Maxwell's equations imply $H = [\sqrt{\epsilon/\mu}]^* E$ (where epsilon and mu are the permittivity and permeability of the propagation medium respectively) and that the refractive index $n = c^* \sqrt{\epsilon\mu}$.

This produces the following magnetic field components:

$$H_i = n_1 E_i / \mu_1 c, \quad H_r = n_1 E_r / \mu_1 c \quad \text{for medium 1, and}$$

$$H_t = n_2 E_t / \mu_2 c \quad \text{for medium 2.}$$

Based on the previously described boundary condition for the magnetic field components, this yields the equation:

$$n_1(E_i - E_r)/\mu_1 = n_2 E_t/\mu_2 .$$

This, combined with the boundary conditions for the electric field, yields the following equations for the Fresnel reflection and transmission coefficients:

$$r_p = [(n_1/\mu_1) \cos \theta_i + (n_2/\mu_2) \cos \theta_t] / [(n_1/\mu_1) \cos \theta_i - (n_2/\mu_2) \cos \theta_t] = E_r/E_i \text{ and}$$

$$t_p = [(n_1/\mu_1) \cos \theta_i + (n_2/\mu_2) \cos \theta_t] / 2(n_1/\mu_1) \cos \theta_i = E_t/E_i . \text{ (Lvovsky 2013)}$$

Because the amplitudes E_i and E_t are complex values, the reflection coefficient may be written as:

$$r_p = r_p e^{i\phi} = [\tan(\theta_i - \theta_t) / \tan(\theta_i + \theta_t)] e^{i\phi} , \text{ where } \phi \text{ is the phase change of the reflected field relative to the incident field (the properties of which are determined by the refractive indices of the two media) and } i = \sqrt{-1} .$$

We can see from this relation that in cases where $\theta_i - \theta_t = \pi/2$, the reflection coefficient has a value of infinity, a condition referred to as “resonance”. For situations where this condition is met, it can be assumed that $\cos \theta_i = -\sin \theta_t$ and that $\tan \theta_i = k_{ix}/k_{iy} = -n_2/n_1$. Using these relations and the previously defined k-vector condition of Snell's law, the components of the k-vector can be expressed as:

$$k_x^2 = k_1^2 - k_{y1}^2 = k_1^2 - k_x^2(\epsilon_1/\epsilon_2) \text{ where } k_x = \omega/c \sqrt{\epsilon_1 \epsilon_2 / (\epsilon_1 + \epsilon_2)} \text{ and } k_{(y1, y2)} = \omega/c \sqrt{\epsilon_{(1,2)}^2 / (\epsilon_1 + \epsilon_2)} \text{ where } \epsilon_1 \text{ and } \epsilon_2 \text{ are the dielectric constants of the two media. (Kooyman 2008)}$$

The metallic surface of the boundary possesses a large concentration of free electrons, a component of its nature as a conductor, and is thereby capable of being represented via the so-called

“Free Electron Model.” The free electron model treats this conductive metallic surface as a cloud of negatively charged electron gas with a core of positively charged ions from which a collective of valence electrons has broken away. This dielectric value associated with this modeled free electron gas is: $\epsilon(\omega) = 1 - n e^2 / \epsilon_0 m \omega^2$ where n is the number of electrons per volume, e is the electron charge, m is the electron mass, and ϵ_0 is the vacuum permittivity, while the associated plasma frequency is $\omega_p = n e^2 / \epsilon_0 m$ (the “plasmon” frequency of the metal).

The dielectric function of the metal can now be written as $\epsilon_2 = 1 - \omega_p^2 / \omega^2$, indicating that for cases where the plasmon frequency is greater than that of the wave angular frequency, the metal can be said to have a negative dielectric constant. More specifically, equations

$$k_x = \omega / c \sqrt{(\epsilon_1 \epsilon_2 / \epsilon_1 + \epsilon_2)} \quad \text{and} \quad k_{(y1, y2)} = \omega / c \sqrt{\epsilon_{(1,2)}^2 / \epsilon_1 + \epsilon_2}$$

show that for situations where $\epsilon_2 \ngtr \epsilon_1$, the y-component k-vector becomes purely imaginary but the x-component remains purely real, indicating a field which propagates completely parallel to the interface with only evanescent wave components orthogonal to this direction of propagation, i.e. an SPP. (Kittel 2004)

1.4 Momentum Matching

For the SPP, the x-component of the k vector (the only real component of the k-vector) gives a surface plasmon wave number equation of

$$k_{sp} = \omega / c \sqrt{(\epsilon_1 \epsilon_2(\omega) / \epsilon_1 + \epsilon_2(\omega))}$$

This forms the basis of the dispersion relationship (seen in Fig. 2) between the ratio of the incident EM frequency and the surface plasmon frequency, and the wavenumber. However, as shown in the graph, it

is not possible for free-space electromagnetic radiation to induce a surface plasmon naturally due to the momentum (or k-value) mismatch, implying that electromagnetic radiation on its own cannot provide both the necessary angular frequency and wavenumber to produce the phenomenon. To circumvent this, momentum matching (where the magnitude of momentum “P” is $P = \hbar k$ where \hbar is Planck's Constant) is required. There are a number of methods to achieve this, but the most commonly employed techniques are the Otto and Kretschmann prism configurations, and the grating method (the technique employed in this study).

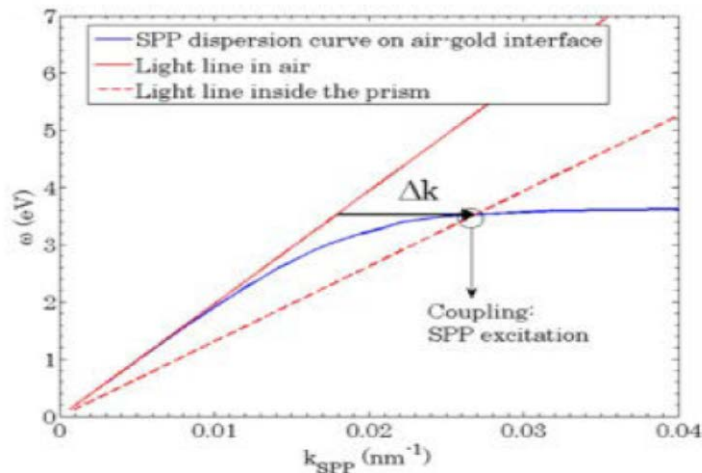


Figure 2: Dispersion relationship between angular frequency and wave number.

Dispersion curve for inducing SPP (blue) naturally does not meet the dispersion for naturally occurring radiation (solid red line), but momentum matching can alter the relationship between frequency and wavenumber for electromagnetic radiation, inducing an SPP (Pitarke et al. 2007)

1.4.1 Kretschmann and Otto Configurations

Both the Kretschmann configuration and Otto configuration are prism methods which utilize the total internal reflection effect to induce an SPP. Total internal reflection is an effect by which a light wave, passing through a higher refractive index material at some critical angle, prevents any transmission of the light through the material, simultaneously producing an evanescent wave

orthogonal to the point of interaction. By passing the radiation through a prism with a high refractive index, the radiation's propagation velocity is altered, thereby changing the momentum of the incident radiation before it reaches the conductive surface.

The Kretschmann Configuration (seen in Figure 3) places the prism directly on the surface of the conductive material, with a dielectric medium (generally air) on the opposite side of the structure. Light with an angular frequency less than that of the plasmon angular frequency which is reflected at the boundary between the conductive metal and the crystal thereby attains a new wavenumber of $k = \sqrt{\epsilon_1}(\omega/c)\sin\theta_i$ for both the incident radiation and the produced evanescent wave which is capable of meeting the surface plasmon requirements at some frequency.

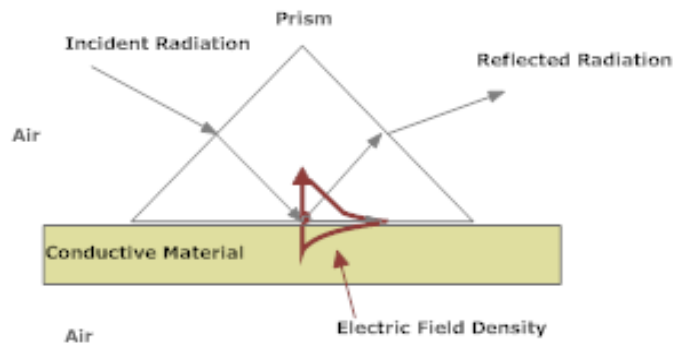


Figure 3: The Kretschmann Configuration

Places the prism used for momentum matching directly over the conductive surface, producing an SPR and associated evanescent electric field at the location of interaction

The Otto Configuration (Fig. 4), on the other hand, places a layer of dielectric material (generally air) between the prism and the conductive surface. In this configuration, total internal reflection occurs at the boundary between the prism and the dielectric, and the resulting evanescent wave penetrates the boundary of the dielectric and metal layers, inducing the SPP. (Toropov and

Shubina 2015)

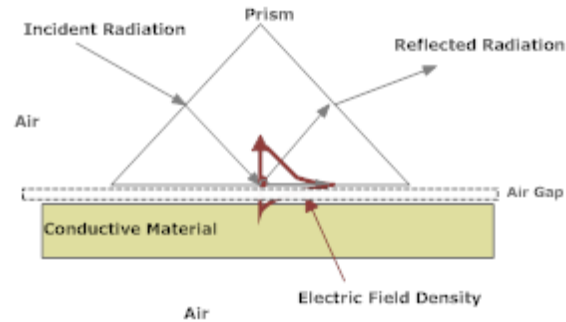


Figure 4: The Otto Configuration

Includes an air gap between the momentum matching prism and the conductive material, inducing an SPP via evanescent wave penetration of the conductive material

However, while both of these techniques are sufficient for producing the desired SPP effect and can be produced on nearly any conductive material, prism configurations are limited in their utility (especially for thermally excited SPP) by the requirements of bulky prisms and the need to alter the position of the prism in order to produce the effect in multiple locations. To get around this limitation, grating structures are often employed in lieu of Kretschmann or Otto configurations.

1.4.2 Grating Method

It is possible to achieve the same effect as the previously described prism methods by use of a periodic, conductive grating surface. When incident radiation interacts with the boundary between dielectric material and the conductive grating, the grating diffracts the radiation into distinct propagation modes (see Fig. 5). The grating wavenumber produced by this diffraction may be expressed mathematically as $k_x = (2\pi/\lambda) \sqrt{\epsilon_1} \sin \theta + m(2\pi/\Lambda)$, where m is the propagation mode (0,

$\pm 1, \pm 2, \dots$), λ is the wavelength of the incident light, and Λ is the periodicity of the grating. For the diffracted mode(s) where $k_x = k_{sp}$, the produced wave vectors will induce a SPP. Previous experiments have shown that the wavelength at which an SPP can be induced is approximately (though slightly greater than) the periodicity of the grating structure. (Radko et al. 2008)

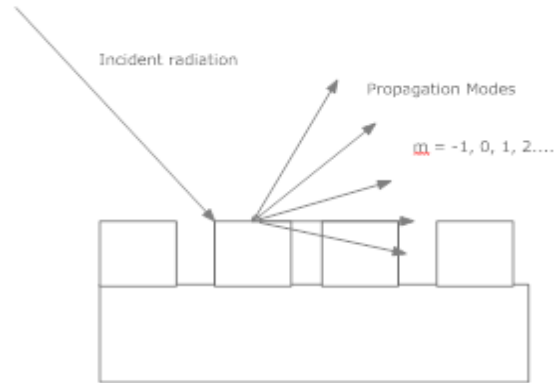


Figure 5: Grating method

In which incident electromagnetic radiation is diffracted into various “modes” of propagation, each mode represented by a different integer

While individual gratings are stationary, they are easy to replicate using current lithography techniques and do not require cumbersome prisms to induce SPP's. This makes them ideal for applications measuring thermal emissions over a wide area or performing a large number of measurements.

1.5 Thermal Radiation and Kirchoff's Law

The primary application of producing an SPP considered in this study is its capability to enhance the emission power of electromagnetic radiation output at specific wavelengths. Any physical object with a temperature above that of absolute zero produces electromagnetic radiation, referred to as thermal radiation (or in some cases “blackbody radiation), in a state of thermal equilibrium with its

surroundings (i.e., no net transfer of heat between the body and its environment). At temperatures such as those seen in the Earth's atmosphere, nearly all this radiation is emitted in the infrared wavelength regions. Using an emissions spectrum like the one seen in Figure 6, this phenomenon can be quantitatively represented by the emission strength as a function of either wavelengths or wavenumbers.

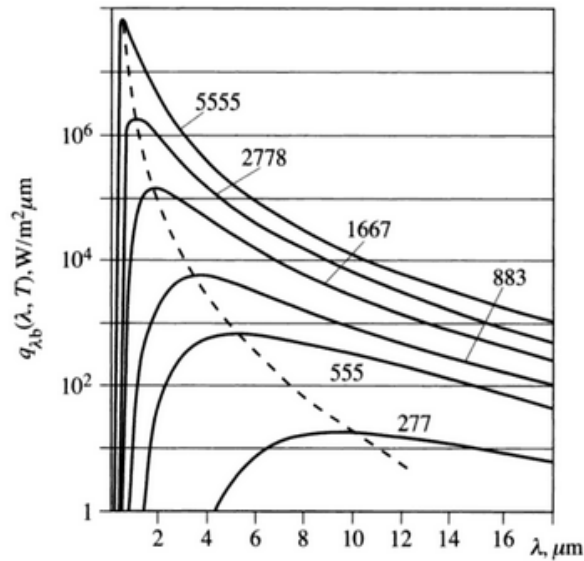


Figure 6: Emissions spectrum of a blackbody ,Spectral radiance flux vs. wavelength (Sharkov 2003)

This radiation is produced by oscillating electrical charges existing on the surface of the body in question, which have been accelerated via thermal motion (motion associated with the object's thermal energy content). These oscillations are only capable of being induced at certain, quantized energy levels, with the total energy of one of these oscillations equivalent to $\epsilon_{osc} = nh\nu$, where n is an integer representing the number of quanta. Max Planck produced a generalized formula to describe the intensity distribution of this radiation as:

$$\rho(\nu) = (8\pi h^3 \nu^3 / c^3) (1 / (e^{(h\nu/k_b T)} - 1))$$

, where h is Planck's constant, ν is the frequency of oscillation, c is

the speed of light, k_b is the Boltzman constant, and T is the temperature in Kelvins. (Oxtoby et al. 2007)

The significance of the SPP with respect to this radiation spectrum can be found in the nature of how the surface electron oscillations are produced: the transference of kinetic energy from the incident radiation photons to the conductive surface electrons. This transfer of kinetic energy can be essentially modeled as the absorption of the incident electromagnetic radiation by the metallic surface, a subject studied intently by Gustav Kirchoff. His efforts yielded a relation referred to as Kirchoff's Law of Thermal Radiation, which states that for a body in thermal equilibrium, there is an identical ratio between that body's absorption and emission characteristics for all wavelengths of electromagnetic radiation. This law, commonly expressed as $e/a = f(T, \lambda)$, where a is the amount of incident radiation absorbed at a specific wavelength, and e is the amount of radiation emitted at the same wavelength, indicates that for wavelengths where an SPP occurs, there should likewise be an increase in emissions for that same wavelength. This connection between SPP frequency and emission enhancement frequency and its potential applications forms the basis of this research and the work done over the past several months. (Schirmacher 2003)

CHAPTER 2 METHODS

The creation of a structure on the order of microns represents a unique challenge in the engineering field. Because traditional tools of construction are too cumbersome directly shape and manipulate materials on the order of 10^{-6} meters or lower, more indirect techniques are required. A wide variety of methods and tools have been developed over the past few decades to create micro-objects and structures on these scales, but for this project a top-down method referred to as DLW, a variation of the more traditional technique of photolithography, was employed.

2.1 Photolithography

Photolithography is a commonly used “top-down” method of micron and sub-micron fabrication. Light-sensitive materials, such as “photoresists,” are unique in nature for their ability to undergo polymerization (negative tone) via exposure to electromagnetic radiation within specific wavelength ranges, rendering them insoluble to water and commonly used solvents such as isopropyl alcohol.

In traditional photolithography (see Figure 7), layers of these materials are exposed to patterns of light within the required wavelength region using photomasks, essentially sheets of opaque material with the desired pattern cut into them. This ensures that the desired shape is projected onto the photoresist layer, initiating the polymerization of the photoresist in a specific pattern. Following this exposure, the sample is then exposed to a heat source, providing the energy required to complete the process of polymerization, and is then placed in a developer fluid solvent, dissolving the photoresist that was not exposed to the radiation pattern and leaving only the desired shape. Upon completion, a technique known as “soft-lithography” follows (see Figure 8 e) and f)), in which the pattern is coated with a layer of elastomeric material (in this case, polydimethylsiloxane or “PDMS”) and cured for three hours at 60°C . This curing solidifies the PDMS and produces the inverse of the pattern it was placed

on top of in the elastomer. The layer is then peeled away from the substrate containing the master pattern, leaving a structure for use in the emission tests. (Zhang et a. 2010)

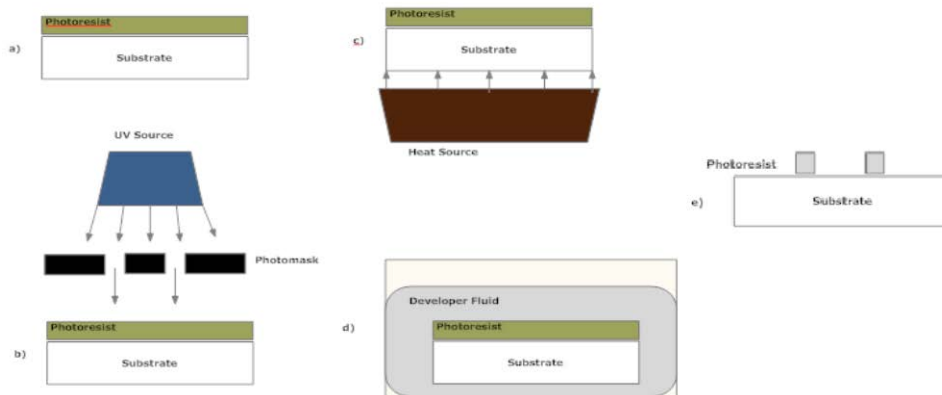


Figure 7: Basic photolithography process
 a) substrate has a layer of negative photoresist added, b) UV light passes through a photomask, c) exposure to additional heat source to complete polymerization process, d) developer fluid exposure removes non-polymerized photoresist, e) with excess resist removed, cross-linked structure remains

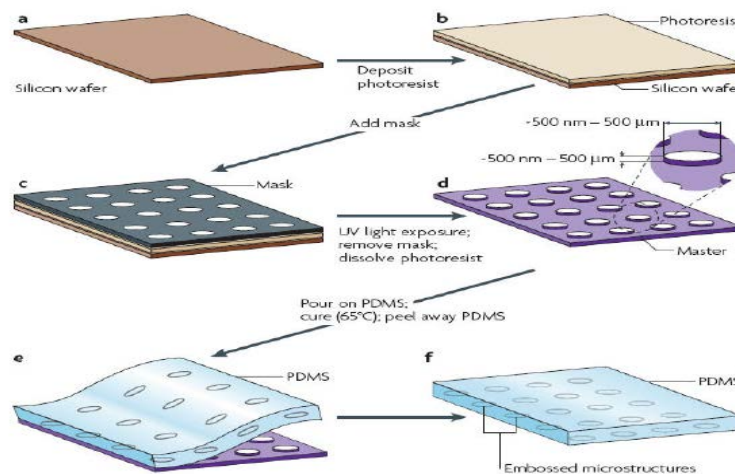


Figure 8: Soft-lithography process
 a)-d) steps from the negative resist photolithography technique, e) & f) application and removal of PDMS elastomer which now carries the inverse of the photoresist pattern (Weibel et al. 2007)

2.1.1 Photopolymerization

The process of photopolymerization is a commonly employed polymerization method via radiation-induced cross-linking. There are several types of known mechanisms of photopolymerization, but the one of greatest relevance to this experiment method is referred to as

“chain-growth” photopolymerization, in which a small group of molecules with bonds weak enough to be broken via light exposure (also called a “photoinitiator”) to produce free radicals, such as anions or cations (negative and positively charged ions respectively). In the SU-8 2000 series of photoresist, a cationic photopolymerization method is employed to initiate the cross-linking process. In the cationic photopolymerization, a photoinitiator is exposed to radiation to release a cation (positively charged ion) which is then used as an active center in the polymerization process. This allows nearby monomers to form repeating links with one another to form the supra-molecule (polymer), a process referred to as cross-linking. The result is a solid layer of “hardened”, insoluble macro-scale polymer. (Crivello and Reichmanis 2014)

However, while photolithography is an effective and common tool used for micron-scale fabrication, the technique is limited in its flexibility. Each individual pattern requires a specific photomask in order to project the desired “image” onto the photoresist and must be moved in order to project this image across an area larger than that covered by the photomask. In order to circumvent this problem, recent advances in the miniaturization of laser equipment has allowed for a variation of photolithography to be employed known as DLW.

2.2 Direct Laser Writing

In traditional photolithography, the photoresist material is exposed to a radiation source within a specified wavelength range (typically ultraviolet) in order to induce a cross-linking process within the photoresist, linking the polymer chains within the material and “hardening” the affected areas (thus rendering them insoluble). As previously stated, this process uses a physical barrier referred to as a “photomask” which blocks all radiation propagation with the exception of the pattern allowed through

pre-cut openings. However, it is possible to achieve an identical effect utilizing a concept known as DLW, in which the necessary radiation is focused to a micron or sub-micron scale focal point to expose only the desired areas to the necessary radiation without the use of a photomask (see Fig 9).

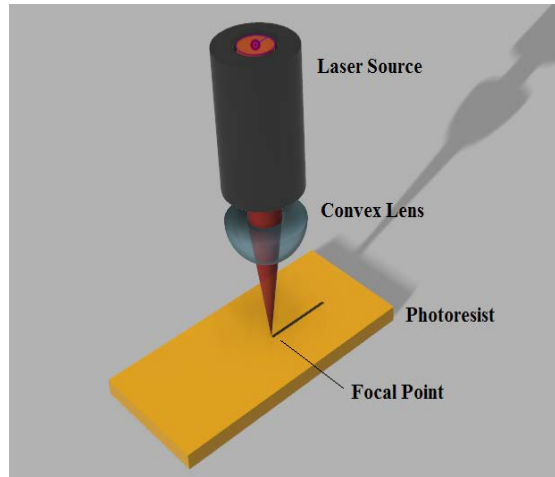


Figure 9: DLW concept

Laser source (in this case a series of mirrors which have reflected the beam pulses from the Mai Tai laser, uses a convex lens used to focus the beam to a high resolution focal point onto the glass substrate containing the photoresist

Each individual pixel is exposed to the beam focal point for an amount of time based on the positioner velocity. The laser employs a Gaussian Beam Profile (Figure 10), with an electric field of

$$E = E_0 \exp(-r^2/\omega_0^2)$$

and an intensity distribution of

$$I = I_0 \exp(-r^2/\omega_0^2)$$

where r is the distance from the focal point center and ω_0 is the Gaussian Beam radius. This profile indicates the energy carried by the photons most likely to be exposed to the photoresist during the time

the pixel is exposed to the focal point.

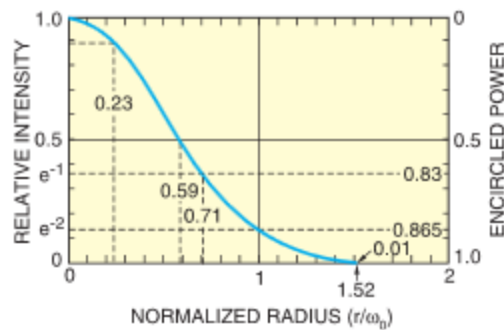


Figure 10: Gaussian Intensity Profile

Intensity is a function of distance from the center of the Gaussian Beam (Newport, “Gaussian Beam Optics)

Photons whose energy exceeds a specific threshold (dependent on the type and thickness of the photoresist) are absorbed by the material to produce the cations for the previously described photopolymerization process. While the time required to produce the desired pattern is greater than simply exposing the entire area to a single radiation source at once, this is offset by the time saved by creating an automated program to repeat the pattern as many times as desired without having to move the photomask, as well as significantly improved writing resolution capability. (Herzig 1997)

2.3 Sputter Coating

Once the basic structure has been formed into the PDMS substrate, it is necessary to coat the

structure in a conductive material, thereby completing the grating necessary to induce an SPP effect. This is achieved by using a technique called “sputter coating,” a process of depositing conductive metals onto a structure via ion bombardment. This is achieved via a kinetic energy transfer, wherein a target (in this case a gold sheet) is eroded by shearing off pieces of the target using charged ionic particles.

An inert gas, usually Argon, is pumped into a vacuum chamber (see Figure 11), with the target to be bombarded placed on top of the chamber under the anode, and the specimen to be coated placed in the bottom of the chamber above the cathode. A negative charge is then applied to the anode above the target material, causing free electrons to break away from the metal and collide with the inert gas atoms. These collisions cause some of the atoms to transition to positively charged ions, producing a cloud of ionic gas (plasma) which is attracted to the opposite-charge anode. These ions collide with the target specimen, eroding the conductive metal and depositing gold particulates onto the sample over the cathode. The current set by the user determines the rate of deposition, as a higher current causes more free electrons to break away from target sample, raising the chances of electron-atom collisions and increasing the number of ions bombarding the target sample. In the case of the Denton Vacuum Sputter Coater used for the experiment, an 80 nm thick layer can be produced via a 3.5 minute exposure to a current of ~50mA. (Quorum Technologies 2002)

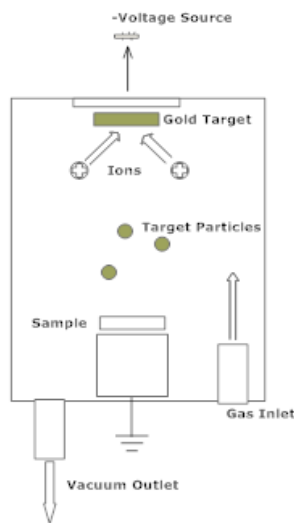


Figure 11: Sputter Coat Concept

A vacuum is created within the chamber before pumping Argon into it. An electric current produces ionized Argon particles, which then impact a gold target, depositing gold particulates on the sample

2.4 FTIR Spectroscopy

Fourier Transform Infrared (FTIR) Spectroscopy is a common method of measuring the emissions spectrum of an object, employing a device referred to as an interference meter (interferometer) to measure thermal radiation within a specific region of electromagnetic spectra (specifically, infrared). Among the most commonly employed interferometers is the Michelson Interferometer (see Figure 12), which employs a collimating mirror, a fixed mirror, a moving mirror, and a beam splitter. The infrared radiation from a local source is transformed into a uniform collection of parallel beams by the collimated mirror before traveling to the beam splitter. The beam splitter then divides the radiation into two separate, perpendicular beams, sending a portion of the radiation towards the stationary mirror, and the remainder towards the moving mirror. The two beams are then reflected back to the beam splitter where they interact with one another via a process referred to as

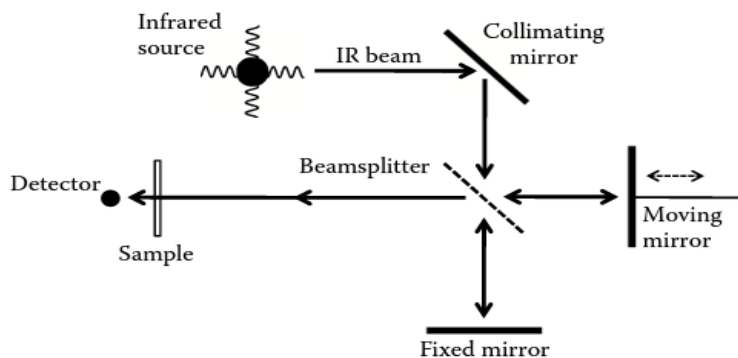


Figure 12: Michelson Interferometer

“interference.”

Figure 12: Optical diagram of a typical Michelson Interferometer (Smith 2011)

Interference is, essentially, the superposition of two electromagnetic waves into a single wave profile via a combination of the two wave amplitudes. In a Michelson interferometer, these amplitudes combine with one another via the following relationship: $A_f = A_1 + A_2$ where A_f is the final amplitude following interference, and A_1 and A_2 are the amplitudes of the beams reflected from the fixed and moving mirrors respectively. In cases where the absolute value of final amplitude is greater than that of either of the original amplitudes, “constructive interference” can be said to have taken place. Constructive interference occurs only in situations where two waves have both identical frequency and an identical phase (location where the wave is in its oscillation when the cycle starts), a state known as “in-phase.” In cases the in-phase conditions are not met, the absolute value of the final amplitude will be lower than one of the original amplitudes, known as “destructive interference.” The amplitude of an electromagnetic wave is significant in FTIR spectroscopy because the square of the amplitude value is equal to the intensity of the radiation, a relation which forms the basis for the measurements taken.

Having one mirror moving and one mirror fixed inevitably leads to differences in the distance

traveled by each beam. This difference, referred to as the optical path distance, determines when constructive and destructive interference take place. In cases where $\delta = n\lambda$ where δ is the optical path difference, λ is one of the wavelengths of one of the collimated light rays light, and n is any whole integer (including zero), the two beams will be in-phase and will constructively interfere, producing a higher strength signal (represented by an increase in wave amplitude), whereas in cases where $\delta = (n + 1/2)\lambda$, the two beams will be out of phase and destructively interfere (representing an overall decrease in signal amplitude). Each of these values represent local maxima (constructive interference) and minima (destructive interference) when plotted on an Intensity vs Optical Distance graph referred to as an “interferogram,” which is modeled on the graph as a cosine wave made of the light wavelength being measured. Final interferograms are composed of the sum of all the interferograms from each individual light wavelength.

The Fourier Transform component of this process takes this final interferogram and decomposes it into a function which corresponds to the superposition of sinusoidal wave functions that make up the plot, which in the case of a cosine wave signal is a series of vertical lines (see Figure 13). Using this information, the spectrometer is able to transform the interferogram into a what's known as a single-beam spectrum. So-named for the fact that the process only uses a single collimated IR beam to collect data, it plots the intensity of the light (using arbitrary units) vs. the wavenumber (uses cm^{-1} units, equal to $10,000/\lambda$, where λ is in microns). This gives us a background spectrum, which can be used to measure the strength of the radiation being output by the sample under test over a wide range of infrared wavelengths. (Smith 2011)

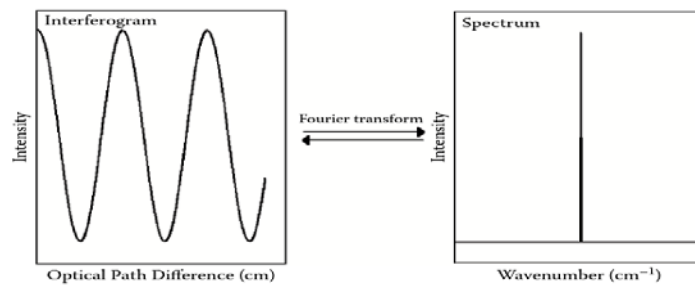


Figure 13: Fourier Transform

Figure 13: Typical Sinusoidal wave Fourier Transform in FTIR spectroscopy (Smith 2011)

CHAPTER 3 PREPARATION AND TESTING

In order to perform the DLW process on a given sample, considerable preparation is required beforehand. A glass substrate (in this case, a 2mm thick glass slide) is manually washed and dried off with an air blower to ensure that no preexisting particulates remain on the sample to interfere with the process. The substrate is then coated with a thin layer of SU8-2005 (~1 mL) using an eye dropper. Once the layer has been applied, the substrate is then placed inside the Spin Coater and spun at 4000 RPM for 30 seconds, in order to ensure the substrate has an initial layer of ~5 μm of SU8-2005.

Once the spin coating has been completed, the sample is placed on a hot plate, pre-heated to 90°C, for 5 minutes to evaporate the solvent (cyclopentanone) which exists in all commercially sold SU8 photoresist material. Once the time has elapsed, the substrate is then put under a UV lamp for 1 minute, initiating a photopolymerization effect to harden the initial layer. This is then followed by a post-bake at 90°C for 5 minutes to complete the polymerization process, and leaving an 5 μm thick adhesive layer for the photoresist material to be patterned to bond to.

For the layer to be patterned (the “pattern layer”), an additional ~1 mL of SU8 are added to the surface of the glass substrate, now coated with the original layer of fully polymerized photoresist material. Spun at 6000 RPM for 30 seconds, this produces a ~2-3 μm thick layer of photoresist, which is then pre-baked to evaporate the solvent. Once this has been completed, the sample can then undergo the DLW process (Micro Chem)

To perform the DLW process, the sample is mounted on the positioners seen in Fig 14 A. The top of the stacked positioners now has a black matte colored platform covered with air columns, upon which the sample is mounted. However, great care must be taken to avoid a coherent back-scattering effect, which in this case is the reflection of light back in the direction it was transmitted which has

passed through a medium at the boundary between the medium and a second medium of a different refractive index. Previous experiments have shown that in cases of coherent back-scattering (such as back-scattering involving lasers) can lead to irradiation of areas near or at the original point of interaction on the surface of the glass substrate. To avoid this issue, the column over which the sample is mounted is first filled with glycerol, which has a refractive index approximately equal to that of the glass substrate, which ensures that back-scattering does not occur when the sample is exposed to the laser. Once the sample has been mounted over the glycerol-filled column, the DLW may proceed. Utilizing the lab's Mai Tai femtosecond laser (690–1040 nm, 80 MHz, 5 Watt max output) a periodic pattern is “drawn” into the photoresist material. (Luna et al. 1995) The entire set-up, including the positioners and laser control system, can be seen in Figure 14.



Figure 14: The Mai Tai DLW Set-Up

- A) The Newport X-Y-Z stage positioners, B) The dielectric mirror, polarizer, and secondary shutter path, C) Mai Tai femtosecond pulse laser**

Following the photoresist patterning, the sample is once again placed on the hot plate at 90°C for approximately 7.5 minutes to complete the polymerization of the area which has been exposed to the UV laser. Once this has been completed, the sample is then placed in a glass jar containing Propanediol monomethyl ether acetate (developer fluid) to remove the portions of the sacrificial photoresist layer which have not been exposed to the UV laser. The sample is once again placed under the UV lamp (this time for 5 minutes) to begin a “hard bake” process to increase the effective strength of the patterned structure and lower the chances of the peel-off process removing a portion of the structure from the substrate. To complete this process, the sample is removed from exposure to the UV lamp and placed on the hot plate for a final time, which has been pre-heated to 200°C and is baked for 15 minutes, ultimately giving the structure an estimated Young's Modulus of ~4.95GPa (Dellmann et al. 1997).

3.1 Control Scheme

In order to perform the DLW process utilized to create the 2-D structure which formed the basis of this research, three considerations had to be taken into account. First, the path of the laser was fixed, so the photoresist sample had to be physically moved beneath the convex focusing lens in order to expose the desired area to the laser focal point. Second, the laser needed to be able to quickly switch off and on to ensure that the only area exposed were those required to pattern a specific shape into the photoresist material by initiating photopolymerization. And third, an appropriate z-axis height needed to be selected in order to ensure that the focal point was small enough to produce a writing resolution that was smaller than the desired periodicity of the structure to be patterned (~5 μm).

3.1.1 Newport Positioners

In order to meet the first and third requirements, a trio of Newport Linear Positioners were utilized to adjust the location of the photoresist sample beneath the path of the laser to produce the desired periodic pattern. These positioners are controlled via a Newport XPS-Q8 Controller, which is capable of being operated in one of two fashions: manual direction via a web-browser user interface, or through pre-programmed coordinate positions or trajectories. This programming may be accomplished in one of two means: the use of the propriety code specific to Newport devices (an inefficient, non-user friendly method), or through a set of custom LabVIEW virtual instruments (VI's) included in the XPS-Q8's internal hard drive and specifically designed to control the positioners. This project ultimately employed these LabVIEW custom VI's to produce a control program.

Producing the desired periodic structure carried multiple requirements: converting image data into a set of coordinates, accepting user requirements for velocity and acceleration settings, and the ability to pattern a single shape multiple times in a specified area. Two programs were written to meet these requirements. Shown in Figure 15, the first program accepts shape, speed, acceleration and jerk time settings from the user. Because the structure desired for this project were two-dimensional, no variation in power output from the laser was required besides the input settings “off” and “on.” As a result, the program required the user to input a bitmap (monochromatic) image file containing a pixel-map representation of the shape to be patterned periodically on the photoresist material. Each individual pixel in a bitmap file has a mathematical value of either 0 or 1 (with the actual image represented by a patterned collection of 1's surrounded by 0's representing “null” space), which can be used to represent either “on” or “off” for the laser's output in a given X-Y coordinate.

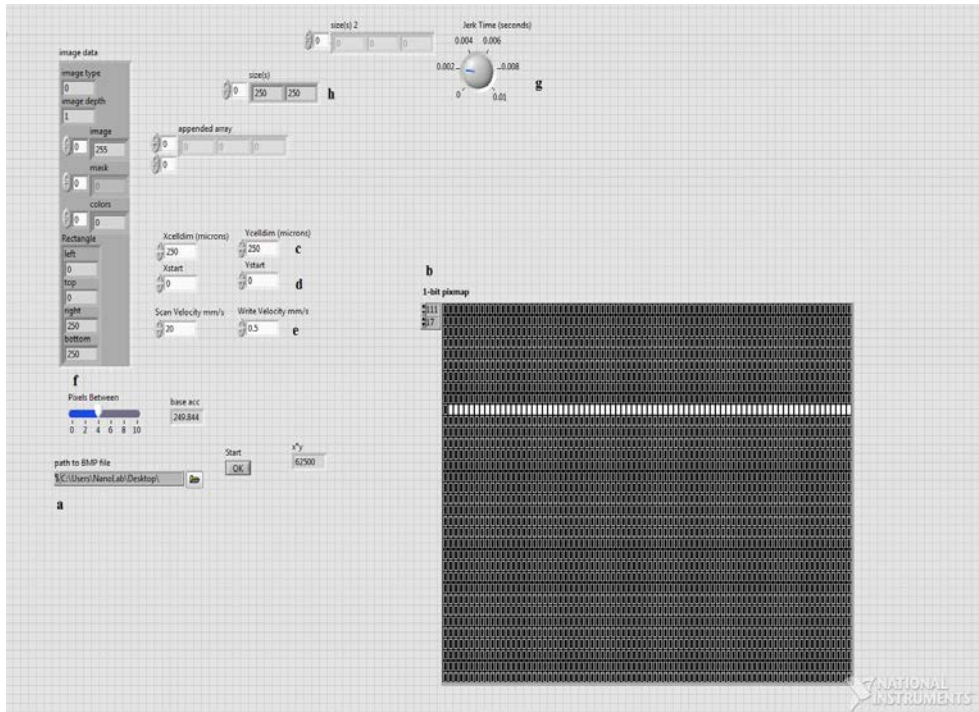


Fig 15 The first of the two programs created to produce a .csv input file to control the positioners: a) the image file to be mapped, b) a pixel map representation of the image (black pixel represents 0, white represents 1), c) the physical dimensions represented by the image in micrometers, d) the x and y coordinate start positions, e) the two positioner velocity settings, f) the number of pixels between the scan and write velocity used to decelerate, g) the jerk time set to lowest possible value for positioners of 0.02 to ensure positioners achieve required acceleration quickly enough, and h) an indicator of the number of x-y pixel dimensions of the image, which is used in conjunction with c) to determine the dimensions of each individual pixel

Figure 15: Custom LabVIEW Program 1 GUI

In order to translate the pixel-map coordinates into real physical positions, the program also requires two additional pieces of data from the user: an X-Y start position for the positioners (traditionally set to [0,0]) and the dimension of the area represented by the image. This information is used by the program to determine the dimensions of each individual pixel, and their position relative to the designated start position. As a result, the pixel-map is read by the program as a set of X-Y coordinate values and saved to a comma separated value file (.csv), along with the accompanying pixel value (0 or 1). This is later read as an instruction to either turn (or keep) the laser on or off upon the positioner reaching designated positions.

The program also requires the user to input desired velocity, acceleration and jerk time setting. Two inputs are required for the velocity settings: a “Scan” speed (defined as the velocity the positioner should be moving at when the laser is off) and the “Write” speed (the velocity when the laser is on). However, due to the difficulty in determining exactly what acceleration value is appropriate to achieve a smooth transition between “Scan” and “Write”, the required user data is instead requested in the form of the desired number of pixels between the starting and ending of the deceleration process. Using this information, the previously requested velocity and jerk time settings, and the basic motion equations:

$$x(t) = x_i + v_i t + 1/2 a t^2$$

$$t = (x / [(v_i - v_f) / 2]) + t_{jerk}$$

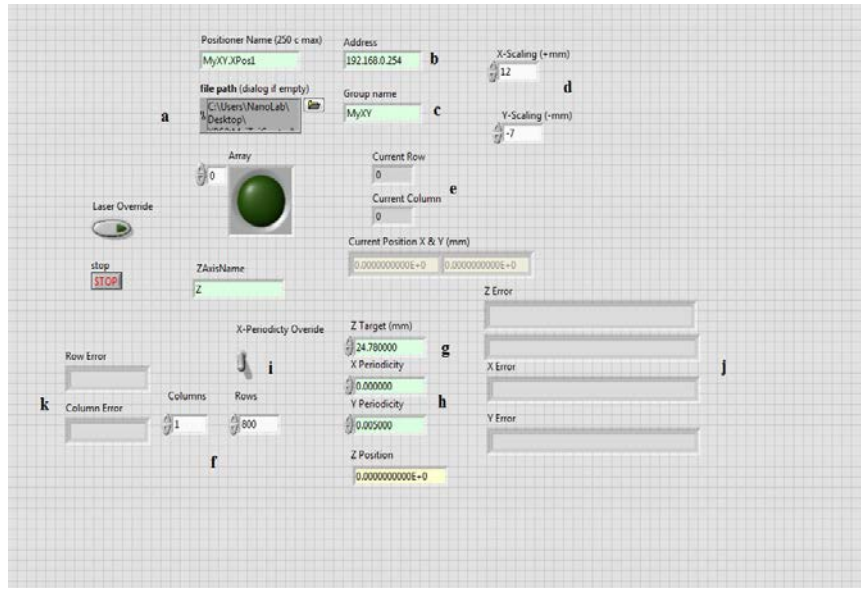
where x is the distance required for deceleration (determined by user inputs for number of pixels to decelerate and the x-y millimeter dimensions of the area represented by the pixelmap in the real world) and t is the total amount of time required to decelerate (based on the average velocity over the entire deceleration and the user input jerk time), the program automatically determines the required time and acceleration rate necessary to achieve the transition between the two velocities in the requested number of pixels. These settings are also saved in the previously mentioned .csv file, to be read by the XPS-Q8 to control the required positioner settings.

Among the more significant challenges in writing this program was decreasing the volume of unnecessary data saved to the .csv file. In a bitmap image containing a single shape (in this case a single line) most of the pixel map contains unnecessary pixel and coordinate data which slows down the writing process and substantially increases the time required for the photopolymerization initialization process. To remove this redundant information, the program is designed to read the pixel map as a series of rows, and automatically deletes all rows that do not have any pixels with a value of

1. In addition, for rows which do contain image data, all pixels following the last pixel with a value of 1 are deleted. This ensures that the only pixel data saved to the .csv file are those pixels necessary for writing the shape (either as a position for turning the laser on, or as a position necessary as part of the positioner deceleration process).

The second program has been designed with a dual function in mind: to utilize the .csv file to control the linear positioners used to move the photoresist-covered glass substrate beneath the laser, and to control a secondary, external shutter used to switch the laser between “off” (0) and “on” (1). The program, seen in Figure 16, requires a number of user inputs to actually write the shape, much like the first program. Along with designating the .csv file to be used to read positioner movement parameters, the program also requests the user for several other inputs: X and Y scaling, X and Y

periodicity, the number of rows and columns, and the initial Z-Axis height settings.



The GUI of the second LabVIEW program, designed to utilize .csv file created from the first program to control the positioners: a) the file input for the .csv file, b) the IP address to communicate with the XPS-Q8, c) the assigned “group” of the positioners controlled, d) the X and Y scaling to move the positioners to the desired initial start position, e) an indicator to show how many rows and columns have been completed, f) the desired number of columns and rows to be produced, g) the Z-Axis height setting, h) the X and Y periodicity settings, i) the override switch to prevent the X-Periodicity setting from interfering with single column arrays, j) the error indicators if a user input is outside the controller parameter setting limits, and k)

Figure 16: Custom LabVIEW Program 2 GUI

error indicators in the event the number of rows or columns takes the positioners outside the position limits

The X and Y scaling inputs add or subtract a designated number of millimeters from the initial

.csv x and y coordinates. These inputs are used to select the appropriate starting position for the array to be constructed, adjusting the initial array coordinates (and all future array coordinates) based on the location of the glass substrate relative to what the positioners consider to be their “home” position (0,0). All future values of x and y have these values added or subtracted from the .csv file to ensure that the pattern shape and size is constant, but in the appropriate location.

The user is also required to enter periodicity values for the X and Y directions. The .csv file produced by the previously discussed program saves, along with all the necessary position, velocity, and acceleration data, the X and Y dimensions entered by the user to determine the length and width of each individual pixel. These values serve as limits for the periodicity, with values below these numbers prompting an error message from the program requesting a new periodicity value. However, there are instances where this limit is not necessary, such as producing a line grating structure with only one column. For these situations, two switches have been added to the program: “X-Override” and “Y-Override.” These switches allow the periodicity limit to be overridden and periodicities less than the X or Y length to be entered.

In conjunction with the periodicity values, the program also requires that user enter the number of shapes to be drawn. This is determined by the “columns” and “rows” buttons (effectively the X and Y dimensions of the 2D array to be drawn). The program draws the initial shape, then reads the .csv file again, only this time adding the entered X periodicity (multiplied by the current column starting from zero) to each of the original x-coordinate values. Once the row has been completed, the Y-Periodicity (multiplied by the current row starting from zero) is added to the y-coordinate values, and the column writing process begins again on the new row. This is repeated until all designated rows and columns of the 2D array have been completed.

Additionally, the user is asked to input a z-axis height for the Laser Write process to be performed at. This is arguably the most critical step, since the z-axis determines the focal point diameter, and therefore, the resolution at which the shape can be drawn (in the case of this experiment, ~ 1 to $2\ \mu\text{m}$). However, this value can be difficult to determine. The material thickness varies every time a new layer of photoresist is applied to a glass substrate via spin coating, and a height change of even $1\ \mu\text{m}$ can significantly alter the focal point diameter. It is therefore necessary to determine the appropriate height setting prior to starting the process for each individual sample.

To find the appropriate value, an initial mark is scratched into the material on a portion of the slide which will not be used to draw the shape. The z-axis is then manually adjusted using the browser-based user interface until the scratch is clearly visible. The position of the slide is then adjusted by $0.5\ \text{mm}$ on the x-axis and the laser is manually activated to determine the profile of the focal point using the mounted ThorCam digital camera. The height is then once again manually adjusted on a micron scale using the web-browser user interface until the focal point diameter is as small as possible. This final height value is then entered into the controller program as the z-axis setting for the DLW procedure.

Once all required information has been entered into the graphical user interface (GUI), the program proceeds to draw the shape. Using the pre-defined movement parameters, the XPS-Q8 moves the positioners beneath the laser while simultaneously switching the laser between “off” and “on” by closing and opening the secondary shutter. Once all required portions of the sample have been exposed to the laser, the program automatically stops and closes, allowing the user to remove the sample and perform the previously described post-UV exposure bake procedure.

3.2 Peel-Off and Sputter Coating

Once the grating structure has been completed, it is time to produce the inverse of the structure in a PDMS sample. First, the glass slide containing the grating is placed underneath a custom designed mold (see Figure 17) to produce a consistent shape in all experiments. Then, a quantity of PDMS (~4.5 grams) is prepared by mixing 10 parts Sylgard 184 Base to 1 part Sylgard 184 curing agent (Dow Corning) to produce a PDMS gel. This gel is then poured into the mold and placed in an oven at 60°C for 3 hours in order to cure, transitioning the material from a gel to a flexible solid. Once the time has elapsed, the sample is removed from the oven and peeled from the SU-8 photoresist grating, leaving an



Figure 17: PDMS mold

inverse pattern on top of the PDMS sample.

On top of grating master pattern

This step is followed by placing the sample within the Denton Vacuum Sputter Coater (see Figure 18). A vacuum is created within the chamber and a supply of argon gas is then pumped inside. By running an electric current through the gas to produce a plasma, gold is deposited on the surface of the PDMS sample for 3.5 minutes, producing a ~80 nm thick layer of gold atop the grating structure.

The final result is a gold-coated, flexible elastomeric structure, capable of undergoing significant elastic deformation (see Fig 19). Once completed, the sample is ready for emissions testing. (Sputter Coating Technical Brief)



Figure 18: Denton Vacuum Sputter Coater

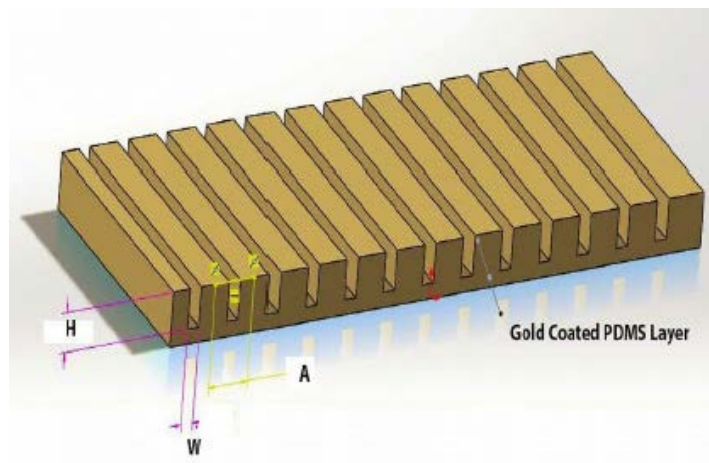


Figure 19: Gold coated elastic grating

Modeled as a semi-infinite with an “infinite” grating length, with “H” height, “W” width, and “A” periodicity

3.3 Uniaxial Strain Due to Bending

Due to the thickness of the samples which undergo emissions testing and their Young's Modulus, it was decided early on that it would be impractical to apply uniaxial strain to the samples by the use of tension applied in the direction of periodicity. To get around this problem, the sample was compressed using a pair of linear stages in order to undergo pure bending, which is capable of producing an axial strain on the side of the sample in the same direction as the change in height of the sample undergoing bending. Seen in Fig. 20, an idealized beam bending scenario yields the following equations for applied axial strain:

$$L' = (\rho - y)\theta$$

$$\delta = L - L' = (\rho - y)\theta - \rho\theta = -y\theta$$

$$\epsilon_x = \delta/L = -y/\rho \quad \epsilon_m = c/\rho \quad \epsilon_x = (-y/c)\epsilon_m$$

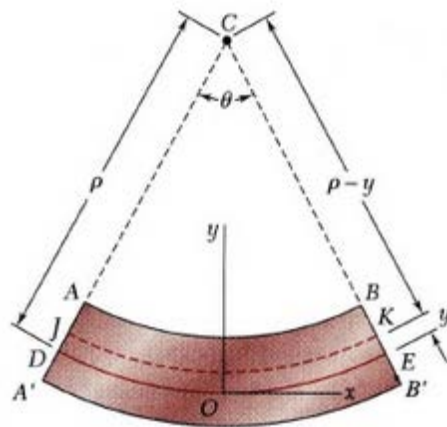


Figure 20: Bending

Figure 20 A beam undergoing pure bending (Beer et al. 2002)

These equations, combined with the following equations based around calculating the degree of curvature (with the neutral axis length treated as the arc length), offer a means of indirectly measuring

the strain applied to the grating with the information offered by camera images:

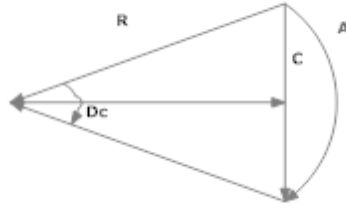


Figure 20a: Bending Curve

$$R = (180A / D_c \pi) = (c/2) / \sin(D_c/2)$$

These equations allowed for an indirect measurement of the strain applied via bending, using dimension measurements taken from a series of digital camera photos for each applied uni-axial stress.

CHAPTER 4 RESULTS

Through a series of trial and error, a 7mm x 7mm final master pattern was produced using the following settings for the DLW set-up: a laser power setting of 0.15 mW and a velocity setting of 2.5 mm/sec. Each pixel was treated as a $\sim 35.5 \mu\text{m} \times 1 \mu\text{m}$ area, so each pixel had an exposure time of ~ 14.2 ms, and therefore an energy exposure of $21.3 \mu\text{J}/\mu\text{m}^2$. In the interest of producing a grating with the smallest periodicity possible (and thereby as close to the wavelength region of highest spectral power at 200°C), the z-axis height was set to 23.80 mm in order to decrease the focal point diameter to its smallest possible value (approximately ~ 1 to $1.5 \mu\text{m}$). This allowed for the production of a grating with a $5 \mu\text{m}$ periodicity and a channel width of ~ 1 to $1.5 \mu\text{m}$, seen in Figure 21 which was used to produce all samples used in the emission testing.

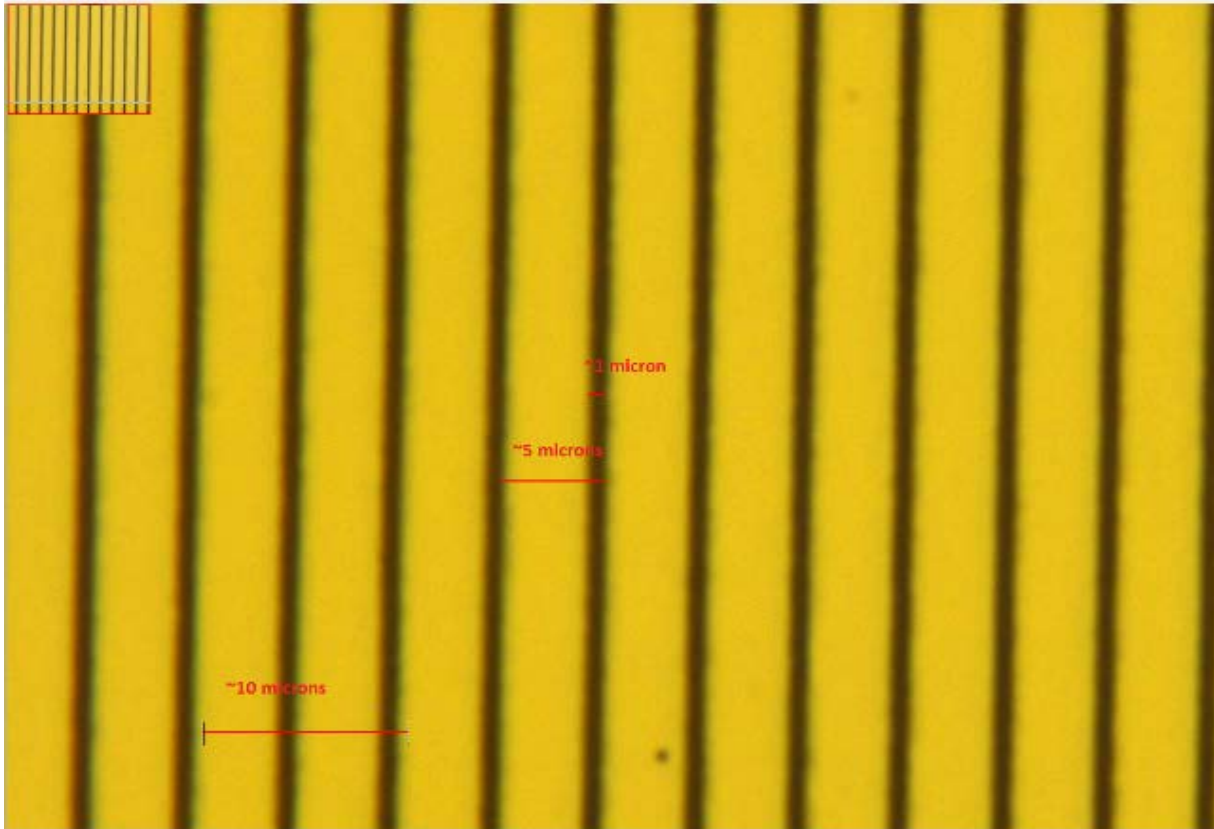


Figure 21: Gold-coated grating
Made from master pattern (10 μm scale in lower left)

Scans performed with an SEM (see Figure 22) revealed a grating height of approximately ~ 2.25 μm , consistent with the thickness of the original sacrificial layer of photoresist material. This height was selected to decrease the chance of the grating ridges merging while undergoing the sputter coating process.

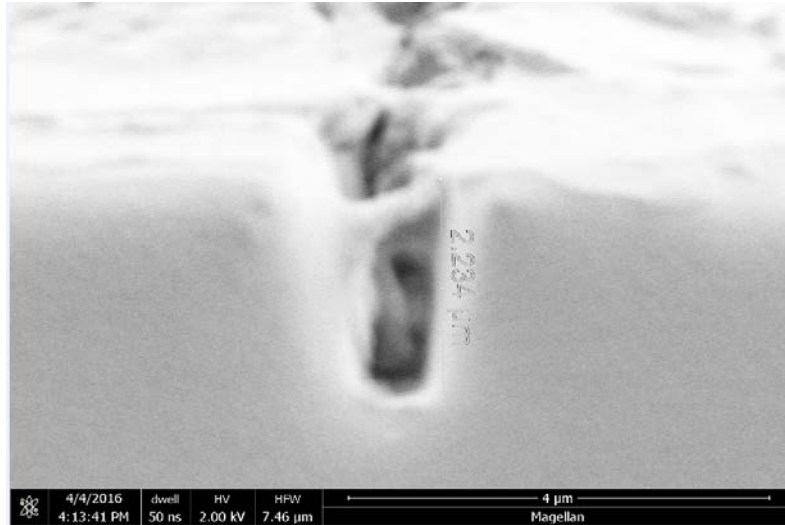


Figure 22: SEM
SEM image of a single PDMS grating ridge

4.1 Crack Testing

It was anticipated prior to the start of the project that the gold layer would undergo significant cracking during the emissions testing. Commercial elastomers have the capability to undergo strains of up to 200% to 300% elastically, significantly greater than that of solid gold, and due to the extreme difference in the quantity of gold and elastomer (~80 nm thick layer vs ~2.5 to 3.0 mm thick layer) it was immediately obvious that the gold would not impede the strain applied to the grating structure. (Goulbourne et al. 2006) As a result, one of the objectives of this project was to verify that the formation and location of cracks formed could be controlled and confined to the space between each of the individual ridges in the grating structure.

It is a long established fact in the field of material mechanics that brittle fracture cracks exclusively form perpendicular to the direction of applied tensile strain. (Que et al. 2015) Because the strains were applied in the direction of periodicity, it was assumed that the resultant cracks would be

limited exclusively to the length-wise direction of the individual gratings. The goal of the first component of testing would be to observe and measure this cracking and, and to then determine its effect it would have on the formation of SPP. Shown in Fig 23a and 23b, the sample was strained as much as could be allowed by the linear stages for the sample length (~140% strain), while being observed under a microscope. However, as shown in Figure 24, it was not possible to observe any cracking in the space between the gratings, most likely due to the height of the individual gratings casting shadows over these spaces, even at the maximum applied strain.

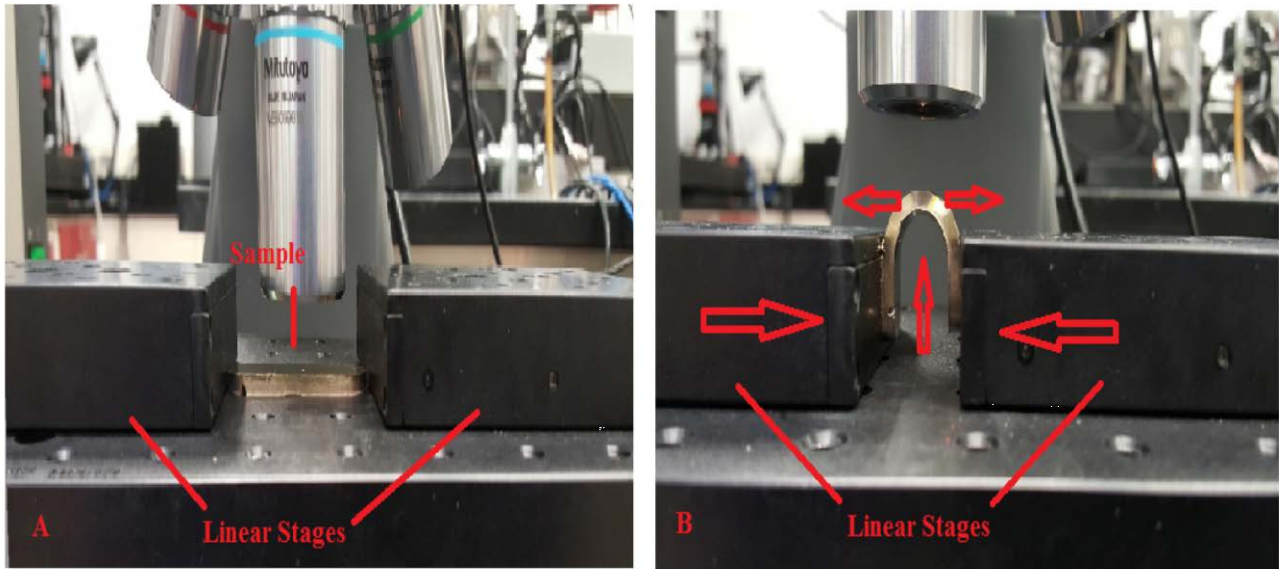


Figure 23: Crack Testing

Samples under strain for crack testing, A) sample at zero applied strain, B) sample at maximum applied strain (~140%)



Figure 24: Crack Test Results
Gold-Coated sample under maximum strain. No crack formation is immediately visible (5 μ m scale in lower left)

However, previous experiments performed with 100nm thick gold layers have shown that crack formation should begin to occur at strains as low as 20% for gold layers of nanoscale thickness, and become the dominant feature of the gold layer around 60% strain. (Midturi 2010) Therefore, it may be reasonably assumed that non-visible crack formation is occurring between the gratings. Moreover, because no cracks are visible on the surface of the grating ridges themselves, it can be further assumed that this crack formation is limited to the regions between each ridge. Strain under an SEM might offer observational evidence of this conjecture in further experiments.

4.2 Characterization of Thermal Emissions

Following the attempt to observe crack formation under high strain, thermal emission tests were performed to determine what, if any, changes in the emission spectra could be observed due to applied strains. Two testing orientations were employed: one (seen in Figure 25 B) placed the sample on a linear stage parallel to the testing table, with the applied compression straining the sample upwards, and the second (see Figure 25 A) with the sample oriented perpendicular to the testing table (a change made necessary due to an alteration in the spectrometer's collecting mirror set-up). 8 sample data sets were ultimately determined to have yielded usable results after undergoing FTIR spectroscopy at $\sim 200^{\circ}\text{C}$. Using the spectrum graphs produced by the tests, the data was converted into a series of .csv files containing the emission data for each wavelength tested at different uni-axial strain values. Using the Origin plotting software, this data was converted into a series of contour plots in order to offer an intuitive picture of the emissions spectra being produced by the samples at different temperature and strain values, with the spectral radiance values normalized on a scale of 0 – 1 (by dividing the emissions of each spectrum by its maximum value) in order to make it easier to determine general enhancement trends.

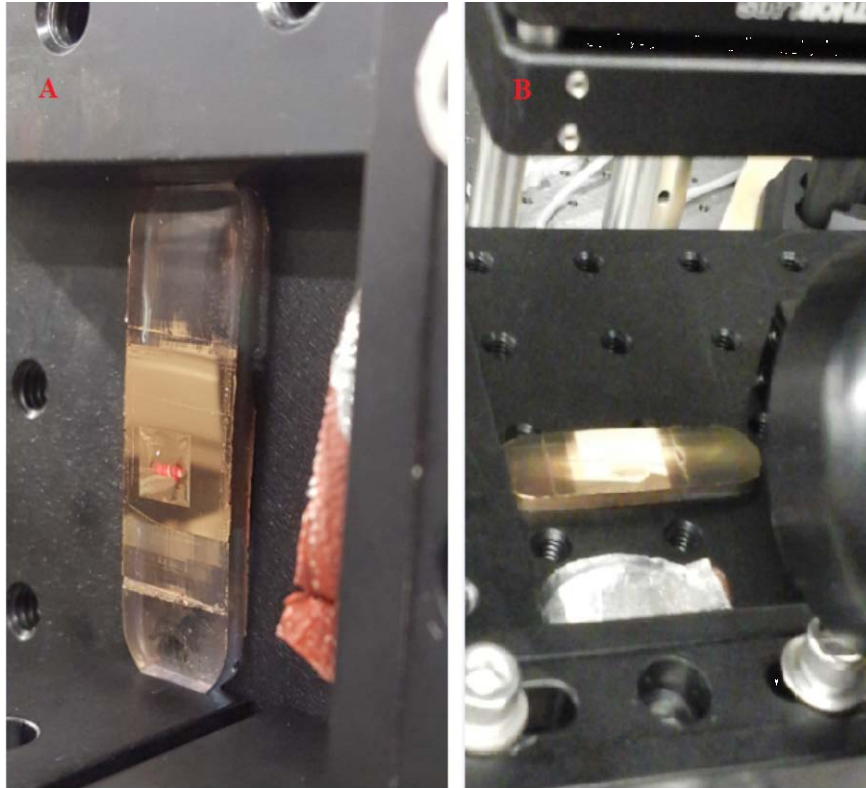


Figure 25: Test Orientations

Test Orientations for Emission Readings, under the IR laser beam and exposed to a dry-air heat source via an air hose, A) Perpendicular orientation used for 5 of the measured samples, B) Parallel orientation used for 3 of the samples

One of the data sets (see Figure 26), the 4th sample produced using the master pattern, serves as a representative example of one of the two spectrum behaviors observed during testing. The graph employs a color-scale to display the relative emission strength of each wavelength, starting with the spectrum for pure PDMS, then pure gold (no grating structure), followed by the spectrum for the grating structure at several strain values (starting from 0 strain). Sample 4 demonstrates a spectrum enhancement behavior that occurs in 3 other emissions test: a red-shifting of the wavelength value for peak emission as more strain is applied. Starting with a region of peak emission centered at 6 μm , applied strain begins to shift the region to higher wavelengths, with the final region of peak

enhancement centering at $\sim 7 - 7.5 \mu\text{m}$.

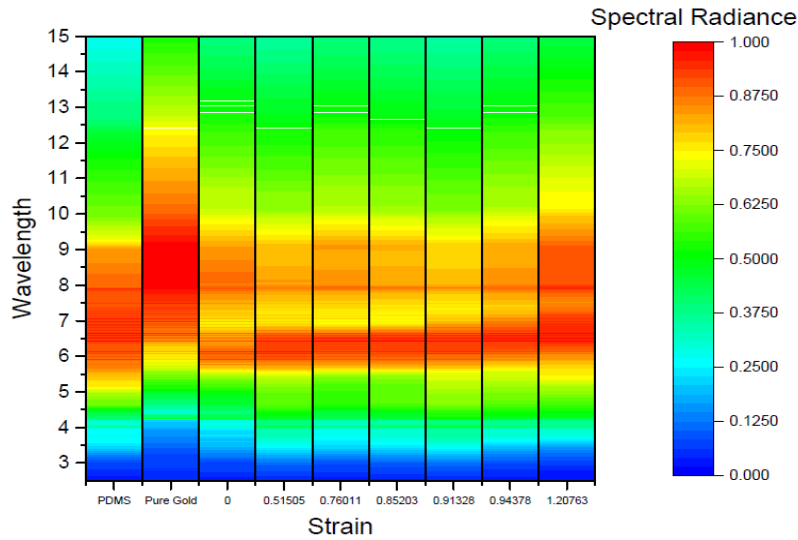


Figure 26: Sample 4 emission contour plot

Each X-Value represents a different applied strain, while each Y-Value represents a different wavelength in the electromagnetic spectrum. Initial peak region occurs with a center of $\sim 6 \mu\text{m}$, later peak region centered $\sim 7 \mu\text{m}$

Another data set (see Figure 27) from the 19th sample produced from the Master Pattern may serve as a representative example of the other trend seen in the emissions spectra of the tested samples: an overall broadening of the region of emission enhancement. An initial emission enhancement in the expected region of $\sim 5.5 - 6.5 \mu\text{m}$ (centered at $\sim 6 \mu\text{m}$) is followed by a broadening of the overall region of enhancement, until it extends from $\sim 4.0 - 7.5 \mu\text{m}$. Interestingly, the center of the enhancement region remains static at $\sim 6.5 \mu\text{m}$. Also of note is an unexpected region of emission enhancement at the $9 - 10 \mu\text{m}$ wavelength region which cannot currently be accounted for.

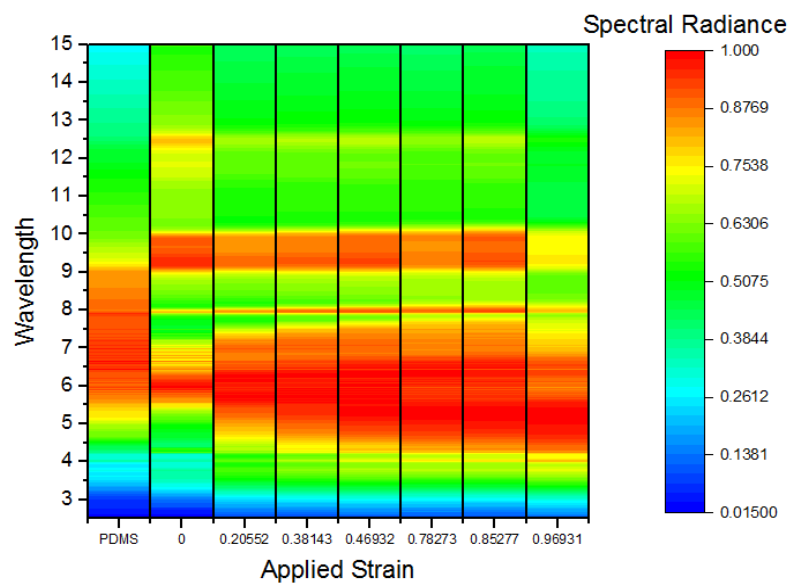


Figure 27: Sample 19 emission contour plot

Each X-Value represents a different applied strain, while each Y-Value represents a different wavelength in the electromagnetic spectrum. Initial peak region of the grating structure occurs with a center of $\sim 5.5 - 6\mu\text{m}$, with the region broadening at higher strains

CHAPTER 5 CONCLUSIONS AND FUTURE WORK

The results from the emissions tests showed a clear initial emission enhancement at a wavelength near the value of the grating periodicity, a behavior consistent with previous grating-coupled Surface Plasmon Resonance spectral enhancement experiments. However, while strain-dependent emission enhancement behaviors are being seen (the original objective of the study), this behavior can be separated into two trends common to all samples was found as uniaxial strain was applied in the direction of periodicity: either a shifting the location of peak emissions, or a broadening of the emissions enhancement location. While the first trend was anticipated due to the change in grating dimensions brought on by applying strain to the structure, the second trend was not, and represents an unexpected response to the application of uniaxial strain. Additionally, while the region of peak enhancement for a number of samples shifting towards higher wavelengths was initially anticipated, the center of these peak enhancements appear inconsistent with the new grating dimensions. Up to and over 100% strain was applied to the gratings in some trials, which more than doubled the distance between the individual gratings. This increased the periodicity of the grating by about $\sim 1.5 \mu\text{m}$, which should have shifted value of the center of the peak enhancement region by a similar amount. As can be seen in the results section, while the original region of enhancement did shift upwards by approximately ~ 1 to $1.5 \mu\text{m}$, a new enhancement region also began to form at a much higher wavelength as more strain was applied, which cannot be accounted for due to the change in grating dimensions.

While more data must be gathered to definitively explain these behaviors, several conjectures have been considered as possible explanations for these trends. In the case of the unexpectedly appearance of a new wavelength region of emission enhancement for the peak-shifting behavior, it is

possible that the formation of cracks produced emission enhancement at higher wavelengths, producing a new enhancement region. Examination of the data (see again Figures 26 and 27) shows that pure PDMS has an initial emissions peak in the 5 to 10 μm region, and the strain applied to the gold may be allowing radiation from the PDMS to pass through, enhancing regions in a non-predicted way. Also, the possible effect of applied strain on the grating itself must be considered as well to account for the strain-dependent enhancement behavior of Figure 27, in which the region of enhancement is broadened below the initial region of peak spectral emission for pure PDMS, or the grating with zero applied strain. Seen in Figure 24, strain applied via compression caused the tops of a number of the gratings to merge together, potentially reducing the periodicity of the structure within certain regions, which may account for the broadening of the region of enhancement into wavelengths below what PDMS or pure gold were shown to be capable of. It could also potentially be due to structural irregularities due to the cracking of the gold layer or an unexpected complex deformation of the grating structure. Consequently, while the project goal of confirming changes to spectrum emission enhancement was partially met, further study is required to account for the specific behaviors and measure the effect accurately enough to produce a workable strain-sensing device.

Future work should be focused on first determining a method to directly observe and quantify the cracking behavior occurring as a result of uni-axial strain. While it may be considered reasonable to assume that a) cracks are forming perpendicular to the direction of the applied strain, and b) the formation of these cracks is confined to the space between the individual grating ridges, direct observation is necessary to either confirm or reject these assumptions in order to account for the potential effect on emission enhancement location. If the formation of cracks is confirmed via direct observation, the degree of fracture formation versus the overall trend of emission enhancement may

then be accurately quantified in the interest of producing a strain-sensing device.

Among the more interesting aspects of the results produced by measuring emission spectra was an unexpected potential application of the grating device. The regions of peak emission enhancement consistently took place in the 6 to 10 μm wavelength region, which also happens to correspond to a region of a high attenuation coefficient for gaseous H_2O . (Chapin 2016) This has the effect of considerably weakening the signal strength of radiation which passes through regions containing water vapor. And the omnipresence of water vapor in the earth's atmosphere (varying between 0.004% and 4% depending on altitude) ensures that emission enhancement occurring in this region is limited in its ability to propagate through air, potentially impeding the detection capability of thermal sensor devices at long-ranges, though considerable testing would be required to determine the effectiveness of the structure in such an application. (Chapin 2016)

BIBLIOGRAPHY

1. G. Ruffato, G. Zacco, and F. Romanato, "Chapter 17." *Innovative Exploitation of Grating-Coupled Surface Plasmon Resonance for Sensing*. INTECH Open Access, 2012. 419-421. Print.
2. J.M. Pitarke, V.M. Silkin, E.V. Chulkov, and P.M. Echenique, "Theory of Surface Plasmons and Surface-Plasmon Polaritons", *Reports on Progress in Physics*, 70, 1, (2007).
3. J. Homola, S. S. Yee and G. Gauglitz, "Surface plasmon resonance sensors: review," *Sens. Actuators B54*, 3–15 (1999).
4. Arne Schirmacher, "Experimenting Theory: The Proofs of Kirchhoff's Radiation Law before and after Planck." *Historical Studies in the Physical and Biological Sciences* 33.2 (2003): 299-335. Web.
5. *Sputter Coating Technical Brief*, Iss. 2, Quorum Technologies, U.K., Ashford, Kent, 2002
6. "*Lithography*", Lithography, MEMS & Nanotechnology Exchange, Web. 5 Dec. 2015.
7. N.c. Goulbourne, E.m. Mockensturm, and M.i. Frecker. "*Electro-elastomers: Large Deformation Analysis of Silicone Membranes*", *International Journal of Solids and Structures*. 2609-626 (2006).
8. Jhon M. Wallace,, and Peter V. Hobbs, "Atmospheric Science an Introductory Survey", 2nd ed. Canada: Elsevier, 2005. Print.
9. Anuj Dhawan, Michael Canva, and Tuan Vo-Dinh. "Narrow Groove Plasmonic Nano-gratings for Surface Plasmon Resonance Sensing", *Opt. Express*, 19, 787-813, 2011.
10. Yuji Fujioka, "Infrared Emission Spectroscopy and Its Application to Analyze Non-smooth Metallic Materials Surface", Rep. no. 100. N.p.: Nippon Steel, 2011. Print.
11. Marc J. Madou, "Fundamentals of Microfabrication: The Science of Miniaturization" 2nd ed. Boca Raton: CRC, 2002. Print.
12. James R. Sheats, *Microlithography "Science and Technology"*, New York: Marcel Dekker, 1998. Print.
13. H.D. Espinosa, and B.C. Prorok. "Size Effects on the Mechanical Behavior of Gold Thin Films", *Journal of Materials Science*, 38(20), 4125-4128, 2003
14. Hans Peter Herzig, "Micro-optics: Elements, Systems and Applications", London: Taylor & Francis, 1997. Print.

15. E. Petryayeva and U. J. Krull, “Localized surface plasmon resonance: nanostructures, bioassays and biosensing-a review,” *Analytica Chimica Acta*, vol. 706, no. 1, pp. 8–24, 2011
16. Robert Siegel and John R. Howell, “Thermal Radiation Heat Transfer”, 4th ed. New York: Taylor & Francis, 2002. Print.
17. Y.L. Zhang, Q.D. Chen, H. Xia, H.B. Sun, “Designable 3D nanofabrication by femtosecond laser direct writing”, *Nano Today* 2010; 5: 435–448.
18. Younan Xia and George M. Whitesides, “Soft Lithography”, *Annu. Rev. Mater. Sci.* 1998. 28:153–84
19. Oxtoby, David W Gillis, H. Pat Campion, Alan, “Principles of Modern Chemistry”, 6th ed. Thomson/Brooks Cole, 2007
20. I. P. Radko, S. I. Bozhevolnyi, G. Brucoli, L. Martin-Moreno, F. J. Garcia-Vidal, and A. Boltasseva, “Efficiency of local surface plasmon polariton excitation on ridges”, *Phys. Rev. B* 78, 115115, 2008
21. Alexander I. Lvovsky, Fresnel Equations. In “Encyclopedia of Optical Engineering”, Taylor and Francis: New York, Published online: 27 Feb 2013; 1-6.
22. Rob P.H. Kooyman, Physics of Surface Plasmon Resonance, In “Handbook of Surface Plasmon Resonance”, The Royal Society of Chemistry: Cambridge, UK, 2008
23. Charles Kittel, “Introduction to Solid State Physics”, 8th ed., Wiley: MA 2004
24. Alexey A. Toropov and Tatiana V. Shubina, “Plasmonic Effects in Metal-Semiconductor Nanostructures”, Oxford University Press: Oxford 2015
25. Swaminadham Midturi, “Stress-Strain Behavior of Nano/Micro Thin Film Materials”, *ARPJ Journal of Engineering and Applied Sciences*, Vol. 5, No. 3, March 2010
26. James V. Crivello and Elsa Reichmanis, “Photopolymer Materials and Processes for Advanced Technologies”, *Chem. Mater.*, 26, 533–548, 2014
27. Brian C. Smith, “Fundamentals of Fourier Transform Infrared Spectroscopy”, 2nd ed., Taylor and Friends Group: FL 2011
28. *SU-8 2000 Permanent Epoxy Negative Photoresist*, Micro Chem, Newton, MA

29. L. Dellmann, S. Roth, C. Beuret, G. Racine, H. Lorenz, M. Despont, P. Renaud, P. Vettiger, and N. de Rooij, "*Fabrication process of high aspect ratio elastic structures for piezoelectric motor applications*", in Proc. Transducers 1997, Chicago, 641-644 1997
30. R.E. Luna, E.R. Mendez, Jun Q. Lu, and Zu-Han Gu, "Enhanced backscattering due to total internal reflection at a dielectric-air interface", *Journal of Modern Optics*, Vol 42, No 2, 257-269 1995
31. Newport, "Gaussian Beam Optics", Technical Reference and Fundamental Applications
32. Ferdinand P. Beer, E. Russell Johnston, John T. Dewolf, "Mechanics of Materials", 3rd edition, Eugene, OR: McGraw-Hill, 2002
33. Charles Rhodes, "Infrared Absorption", Xylene Power LTD, <http://www.xylenepower.com/Infrared%20Absorption.htm> 2014
34. Martin Chapin, "Water Absorption Spectrum", Water Structures and Science, http://www1.lsbu.ac.uk/water/water_structure_science.html, 2016
35. DB Weibel, WR Diluzio, GM Whitesides, "Microfabrication meets microbiology", *National Review Microbiology*, Vol 5, No 3, 208-218, 2007
36. Hock-Chye Qua, Ching-Seong Tan, Kok-Cheong Wong, Jee-Hou Ho, Xin Wang, Eng-Hwa Yap, Jong-Boon Ooi, and Yee-Shiuan Wong, "Applied Engineering Failure Analysis: Theory and Practice" Taylor and Francis Group, LLC: FL, 2015
37. Eugene Sharkov, "Passive Microwave Remote Sensing of the Earth: Physical Foundations", Praxis Publishing: UK, 2003